Electrochimica Acta 404 (2022) 139753

Contents lists available at ScienceDirect

Electrochimica Acta

journal homepage: www.elsevier.com/locate/electacta

Critical roles of reduced graphene oxide in the electrochemical performance of silicon/reduced graphene oxide hybrids for high rate capable lithium-ion battery anodes

Yash Joshi, Avinash Umasankaran, Christopher Klaassen, Mohammed AlAmer, Yong Lak Joo*

Robert Frederick Smith School of Chemical and Biomolecular Engineering, Cornell University, Ithaca, NY, 14853, USA

ARTICLE INFO

Article history:
Received 10 November 2021
Revised 15 December 2021
Accepted 15 December 2021
Available online 19 December 2021

ABSTRACT

Silicon/reduced graphene oxide (Si/rGO) composite electrodes have been investigated for the multiple benefits of rGO in providing mechanical integrity to buffer the silicon volume expansion, while maintaining electronic contact with Si to provide a Li-ion transport pathway and to form a uniform solid electrolyte interface (SEI) layer. In particular, we extensively studied the properties of rGO particles that were reduced from three different routes, namely by heat treatment (TrGO), by chemical treatment (CrGO), and by plasma treatment (PrGO), and co-related them to the electrochemical performance of Si/rGO hybrid anodes. Our results revealed that decreased structural and functional group defects in rGO led to a higher initial columbic efficiency (ICE) of 84%, whereas a higher sphericity of rGO particles resulted in a more stable cycle-life performance for Si/rGO electrodes with 93% capacity retention after 100 cycles at 1C/1C rates. We also observed the important role of the electrical conductivity of rGO in the electrochemical performance of Si/rGO at faster charging-discharging rates, resulting in a capacity of 1000 mAh/g at 2C/2C rates.

1. Introduction

Over-dependence on non-renewable energy has led to increasing environmental concern, facilitating extensive research on clean energy and its storage. Lithium-ion batteries (LIBs) are one of the most commonly used energy storage devices with a number of advantages over other rechargeable batteries, such as higher energy density, higher operating voltages, and easier maintenance [1–5]. Despite their extensive use and eminent potential, state-of-the-art Li-ion batteries have not been able to meet the requirements for vehicle electrification, requiring both higher energy and power density with a longer cycle life simultaneously [6–9]. Graphite, the commercial anode for Li-ion batteries, cannot satisfy these energy density requirements because of its limited theoretical capacity of 372 mAh g^{-1}. Therefore, new electrode materials and chemistry that can provide drastically higher energy density are crucial to the adaptation of next-generation batteries to the EV market and beyond [10,11].

From a materialistic point of view, silicon is one of the most promising candidates as an anode material for LIBs, as it possesses the highest theoretical capacity of 4200 mAh/g [12–14]. Furthermore, Si ranks as the 2nd most abundant element in the Earth's crust next to oxygen and is environmentally friendly [15]. Therefore, Si is an ideal candidate for replacing graphite as an anode material in lithium-ion batteries. Unfortunately, the silicon particles undergo significant volume changes (>300%) during the lithiation/delithiation process. The large change in the volume of Si anodes results in loss of contact with the current collector and between Si and the conductive materials, which leads to rapid capacity loss. Another consequence of this severe volume expansion is the continuous breakdown and reforming of the solid electrolyte interface (SEI), which ultimately results in a thick SEI layer that increases the electrode impedance. Additionally, Si suffers from low intrinsic electrical conductivity [16–19].

There are two primary approaches to overcome the consequences of structural collapse due to volume change, namely nanotechnology and carbon coating [20–22]. While the nanoscale structural modulation of Si can improve its mechanical integrity during charge/discharge cycling, the shielding of nanostructured Si with a second phase is considered one of the most promising strategies for simultaneously increasing the electrical conductivity [23,24]. To that end, graphene and its derivatives, such as reduced graphene oxide (rGO), are employed as robust and elastic sub-

* Corresponding author.
E-mail address: ylj2@cornell.edu (Y.L. Joo).

https://doi.org/10.1016/j.electacta.2021.139753
0013-4686/

stances to encapsulate silicon nanoparticles by dispersing Si into the rGO, in which graphene can buffer the volume changes and improve the electrical conductivity of Si active materials [25–30]. Stress evolution in Si/rGO composite has been studied to ascertain the role of rGO in mitigation of volume expansion and the resultant microstructural changes [31]. rGO is usually used as an alternative to pristine graphene, because rGO can be fabricated on a large scale at a relatively low cost and can be synergistically combined with silicon to form cheap nanoporous composites [32,33].

For example, Xiaosi et al. developed a novel method for the preparation of Si nanoparticles intercalated in graphene sheets by combining freeze-drying and thermal reduction and reported an improved performance with a capacity of 1160 mAhg-1 after 100 cycles [34]. Hong et al. reported a novel honeycomb-like silicon/rGO composite that provided high capacity and good cycling stability [35]. Lin et al. reported a novel method to fabricate Si@C/RGO composites with graphene coated on Si particles, which can effectively overcome the intrinsic drawbacks of Si anodes, such as huge volume changes and low conductivity [36]. Sun et al., fabricated an alternating structure of Si and rGO sheets delivering a capacity of 1500mAh/g after 100 cycles [37]. Recently, Meng et al. engineered a novel way to reduce the defects of the reduced graphene oxide via using glucose and using the defect repaired reduced graphene oxide to support silicon nanoparticles which provides 1284.5 mAh/g at 2C [38].

Although various assemblies of Si/rGO nanocomposite structures as potential anodes have been studied, the effect of the quality of rGO on the electrochemical performance is yet to be investigated. There are three main routes for the synthesis of rGO from graphene oxide (GO): namely by heat treatment, by chemical treatment, and by plasma treatment. Each method of reduction of graphene oxide results in the production of rGO with very different properties. However, the desirable properties of rGO, which positively influence Si/rGO composites, are yet to be probed [39]. In the current study, we extensively characterized various commercial grade rGO particles, which were reduced by the three methods mentioned above, and determined their morphology, chemical composition, and other properties such as defects, electrical resistivity, and interlayer spacing of the graphene sheets. Apart from the different modes of reduction of GO, the studied rGO particles also have distinctively different sizes. We then dissected the effect of the properties of rGO to explain the observed electrochemical phenomena such as capacity, initial Coulombic efficiency, cycling behavior, and rate capability. Air-controlled electrospray (ACE) is the method of choice to form Si/rGO composites, offering several advantages such as low cost, scalability, and environmentally friendly [29,40]. For convenience, all samples were named based on their mode of reduction and average lateral dimension. For example, chemically reduced graphene oxide with an average lateral dimension of 7 µm is referred to as CrGO_7.

2. Materials and methods

2.1. Synthesis of Si/rGO composite

rGO powder (0.1 g), CrGO_7 (ACS Materials), TrGO_5, TrGO_20, PrGO_25 (DJ Semichem, Korea), PrGO_7, PrGO_80 (JMC Corp., Korea), and was dissolved in 7.9 g of distilled water and sonicated for 30 min. To this solution, 2 drops of 5% by weight sodium dodecylbenzene sulfate (SDBS) (Sigma Aldrich) solution in water were added and left overnight. Polyacrylic acid (PAA) (Sigma Aldrich) solution was prepared by mixing PAA (0.5 g PAA in 4.5 g of water and stirring overnight. Si nanoparticles (Si NPs) (0.15 g) were dissolved in 1.6 g of water and sonicated for 30 min. To this, 4 g of rGO solution was added, and the solution was stirred vigorously. Finally, PAA solution (0.5 g) was added. The solution was stirred overnight. The final solution was loaded into a syringe and pumped at an infusion rate of 0.03 ml/min onto copper discs of 15 mm kept at a distance of 17 cm. The voltage was set at 25KV and the applied air pressure was 30 psi. This resulted in the formation of directly deposited electrodes at 1 mg/cm^2. The tap density of the as fabricated electrodes was 0.85–0.9 g/cc.

Table 1
Summary of key properties of rGO particles used in this study.

rGO	Size (µm)	Particle Sphericity	I_D/I_G	Atomic (%)		Resistivity (10^{-3} Ωm)
				C (%)	O (%)	
CrGO_7	7	0.53	0.75	78	22	27.4
TrGO_5	5	0.95	1.03	80	20	38.0
TrGO_20	20	0.72	1.33	89	11	12.4
PrGO_7	7	0.55	0.90	88	12	12.6
PrGO_25	25	0.75	0.61	94	6	1.60
PrGO_80	80	0.73	0.65	90	10	1.67

2.2. Material characterization

The morphology of rGO and the electrodes before and after cycling was studied using a scanning electron microscope (SEM, Zeiss Gemini 500). The Si/C distribution was studied using energy dispersive spectroscopy (EDS, Bruker). The silicon content of the electrodes was evaluated via thermogravimetric analysis (TGA TA Instruments Q500). The chemical composition of rGO was investigated by Fourier transform infrared spectroscopy (Bruker Vertex V80V vacuum FTIR) and X-ray photoelectron spectroscopy (Surface Science Instruments SSX 100 ESCA Spectrometer). The defects in the carbon structure were characterized by Raman spectroscopy (Renishaw InVia Confocal Microscope). The bulk resistivity was investigated using a four-point probe (Cascade CP06). TEM images were taken with a *Thermo-Fisher G* F20 S/TEM in bright-field TEM mode.

2.3. Fabrication of half cells

2032 type coin cells were fabricated in an argon-filled glovebox using directly deposited Si/rGO as the working electrode, a lithium metal disk (MTI) as the counter electrode, and a polyethylene separator (2325 Celgard) to test the performance of the half cells. A homemade electrolyte 1 M $LiPF_6$ as the salt with dimethyl carbonate (Sigma), ethylene methyl carbonate (Sigma), and diethyl carbonate (Sigma) were used as solvents in a ratio of 2:4:4 with 10% fluoroethylene carbonate (Sigma) additive inside the half cells. 15–20 µl electrolyte was used for half cells. The electrochemical properties of the cells were characterized by electrochemical impedance spectroscopy (PARASAT 4000, Princeton Applied Research), cyclic voltammetry (CH Instruments, Potentiostat), and galvanostatic charge and discharge cycles (MTI). A voltage window of 0.01–1.5 V vs. Li/Li^+ were applied to the half cells.

3. Results and discussions

Figure S1 shows the visual characterization of the rGO particles used in this study. The digital photographs clearly show that all the rGO particles are very different in terms of structure and packing. TrGO_5 (0.075 g) occupies the least space, whereas 0.075 g of PrGO_7 fills the entire vial. The low-magnification SEM images of the rGO particles used in this study are shown in Fig. 1, and the average size and sphericity of the rGO particles are listed in Table 1. The sphericity was calculated by ImageJ analysis and verified via an in-house developed MATLAB code. Fig. 1(a) shows that CrGO_7 has a high aspect ratio, while TrGO_5 in Fig. 1(b) has a

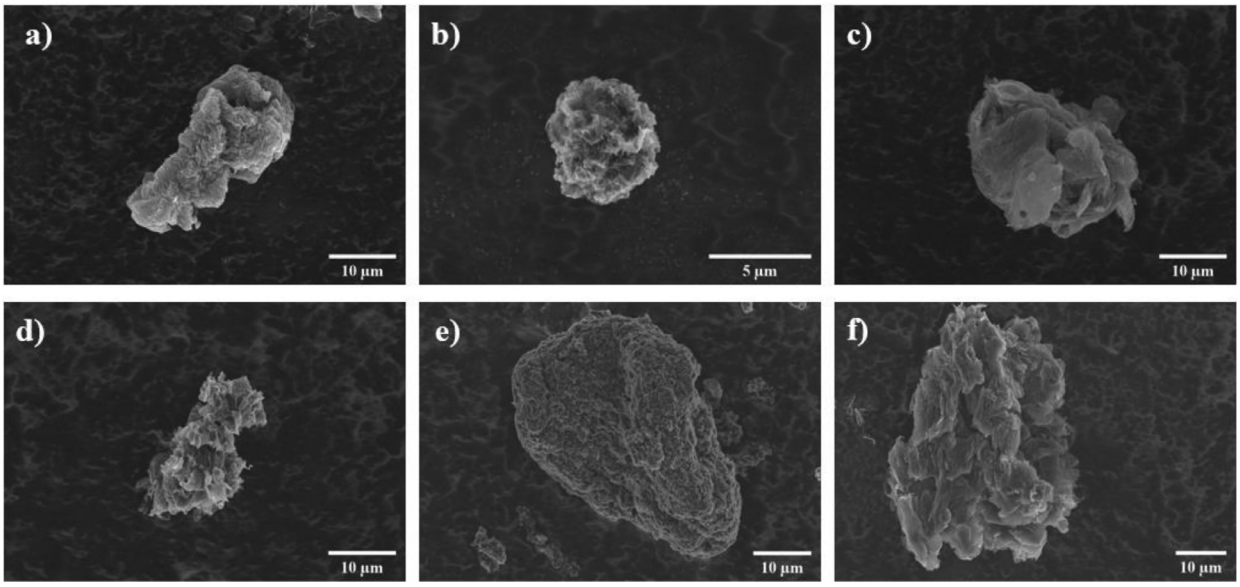

Fig. 1. Low magnification SEM images of a) CrGO_7, b) TrGO_5, c) TrGO_20, d) PrGO_7, e) PrGO_25, and f) PrGO_80.

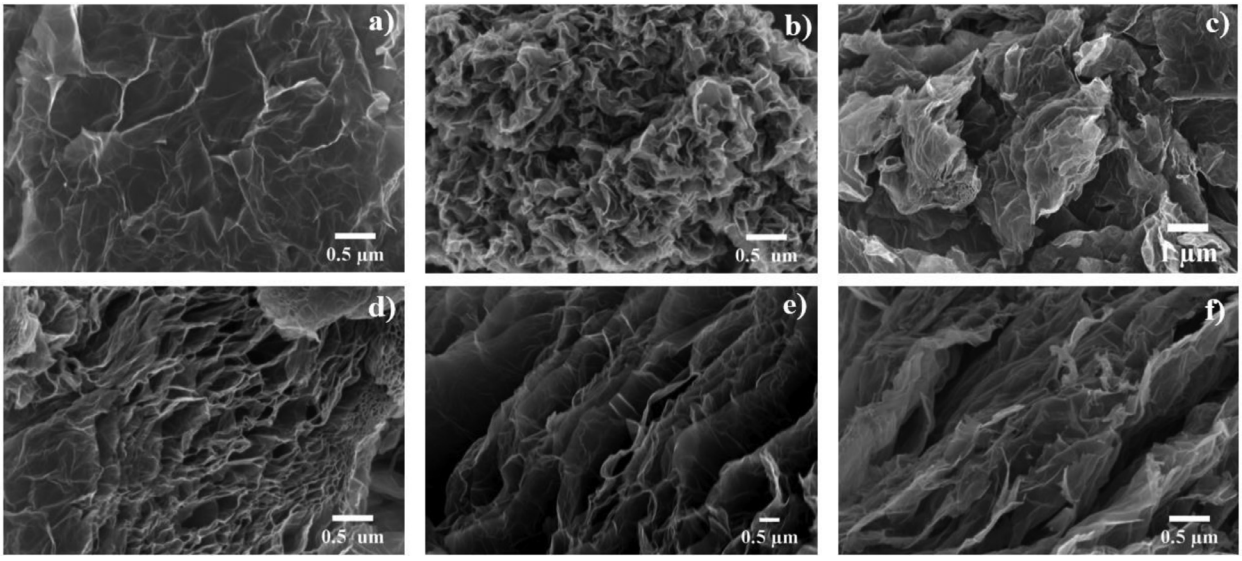

Fig. 2. High magnification SEM images of a) CrGO_7, b) TrGO_5, c) TrGO_20, d) PrGO_7, e) PrGO_25, and f) PrGO_80.

smaller size but has an almost perfectly spherical structure representing a very high sphericity. TrGO_20 (Fig. 1c) is similar to TrGO_5, but has a larger size and lesser sphericity. PrGO_7 (Fig. 1d) has a high aspect ratio and a relatively similar size to that of CrGO_7. As shown in Fig. 1e), PrGO_25 exhibits features similar to those of PrGO_80 but has smaller lateral dimensions. Finally, PrGO_80 (Fig. 1f) has the largest size among all the rGO particles and has a relatively high sphericity. To further examine the morphology of the rGO particles, high-magnification SEM images were obtained, as shown in Fig. 2. While CrGO_7 particles (Fig. 2a) exhibit flattened graphene layers that seem to have been fused during chemical reduction, TrGO_5 and TrGO_20 particles (Fig. 2b) and c) have a highly wrinkled structure, possibly due to shrinkage during thermal treatment. Meanwhile, PrGO_7, PrGO_25, and PrGO_80 particles (Fig. 2d), e, and f) have layered structures with some empty spaces, suggesting loose packing, which seems to be a feature of plasma reduced graphene oxide. High-resolution representative TEM images of CrGO, TrGO, and PrGO are also shown in Fig. 3. CrGO particles (Fig. 3a) exhibit holes and fused graphene layers, while TrGO (Fig. 3b) and c) show severe internal wrinkles, which is in agreement with the high-resolution SEM images in Fig. 2. PrGO particles (Fig. 3d), e), and f) are flatter and smoother than CrGO or TrGO particles, which again corresponds well with the high-resolution SEM images in Fig. 2.

Raman spectroscopy was used to characterize the graphene structure. As shown in Fig. 4(a), all the rGO particles have a *G* band peak at approximately 1595 cm^{-1}, due to the stretching of sp^2 atoms and a *D* peak at approximately 1365 cm^{-1}, due to the breathing modes of sp^2 atoms [41]. Raman spectroscopy is also very useful for characterizing the defects present in the carbon structure due to vacancies [42], sp^3 hybridization [43], and edges [44]. The ratio of the intensities of the *D* and *G* peaks, I_D/I_G, is a measure of the defects present [45] in rGO. In our study, TrGO_20 showed the maximum defects with an I_D/I_G ratio of 1.33, whereas PrGO_20 and PrGO_80 showed the least defects with an I_D/I_G ratio of approximately 0.65. This indicates that plasma reduction leads to reduced defects in the graphene structure. Table 1 lists the I_D/I_G ratios of the rGO used in this study. *The* I_{2D}/I_G ratio shows that all

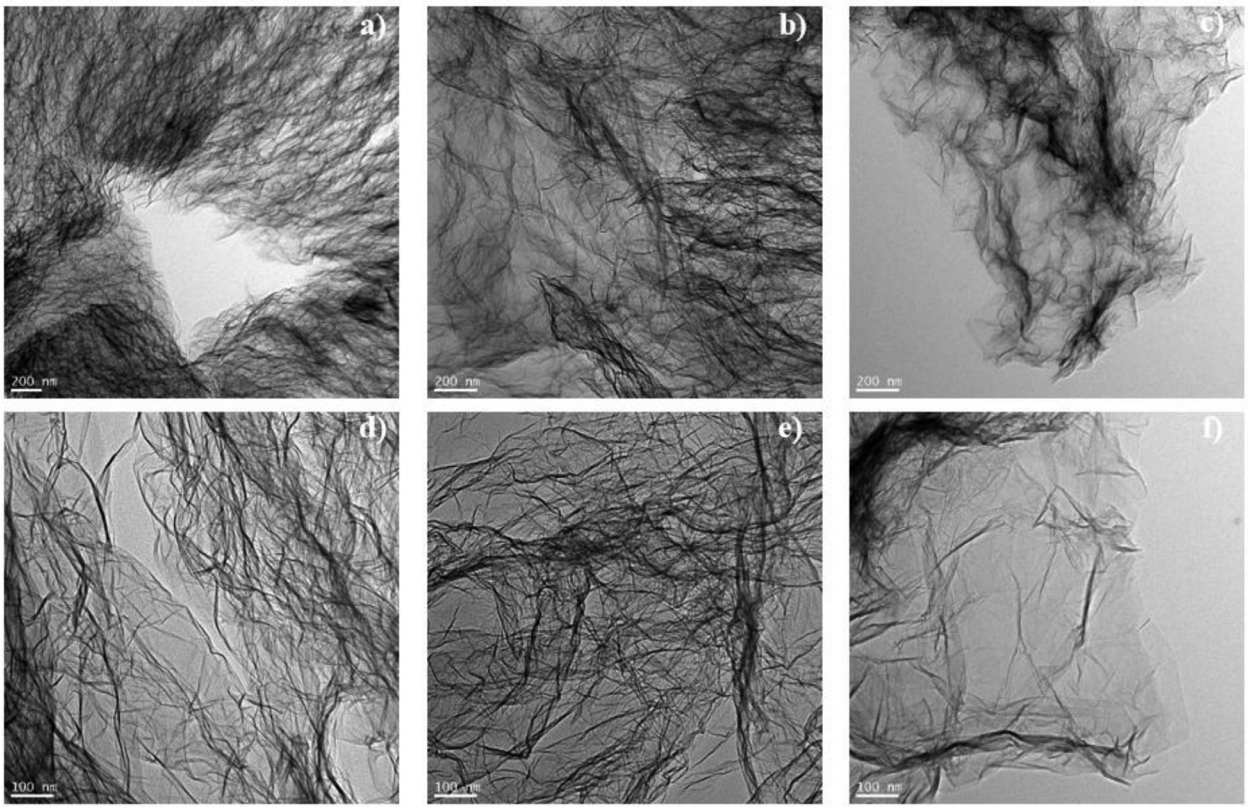

Fig. 3. High magnification TEM images of a) CrGO b) TrGO c) PrGO and high magnification TEM images of d) CrGO e) TrGO and f) PrGO.

the rGO particles used in this study were multi-layered [46]. Next, FT-IR was used to study the effectiveness of the removal of oxygenated functional groups. Fig. 4(b) shows that PrGO_25, PrGO_80, TrGO_20, and PRGO_7 have almost no residual oxygen functional groups, indicating the effective reduction of GO. However, CrGO_7 shows a weak peak representing C = O at 1640 cm^{-1} and TrGO_5 shows a peak at approximately 1250 cm^{-1}, indicating the presence of C–O [47,48]. It should be noted that in Raman CrGO_7, the I_D/I_G ratio is 0.7, which indicates that these defects arise due to the presence of oxygen functional groups, whereas for TrGO_20, with an I_D/I_G ratio of 1.33, defects are structural in nature due to holes or vacancies. XPS is a powerful tool for quantitatively studying the chemical composition of the rGO particles. It is common knowledge that the presence of oxygen functional groups leads to a loss of electrical conductivity of rGO [49–51]. The C% and O% of all the rGO particles used in this study are also summarized in Table 1, revealing that PrGO_25 has 95% C, whereas CrGO_7 has 78.4% C. Fig. 4c) shows the XRD analysis of all the rGO samples. None of the samples had a (001) peak, suggesting effective reduction of graphene oxide. All the samples display a distinct (002) peak at a 2θ value of approximately 25–26° and a small peak of (102) due to the partial removal of the oxygenated functional groups [52,53]. TrGO_5, more specifically, showed wider peaks, possibly suggesting good exfoliation. Additionally, CrGO_7 has the highest inter-planar distance of 3.68 Å suggesting the presence of oxygen functional groups in between the graphene sheets. Fig. 5 shows the resolution XPS spectra C1s for the bonding analysis. All the rGO particles have a characteristic sharp peak at ~ 284.6 eV which represents the C–C bond. Two distinct broad peaks were observed at 286 eV and 288 eV, which represent C–OH and O = C–OH, respectively [54,55]. Table 1 also shows the quantitative bonding analysis for all the rGO particles and, unsurprisingly, PrGO_25 contains the highest% of C–C bonds, in agreement with the survey scan results.

The key properties of the rGO particles used in this study are summarized in Table 1.

These rGO particles were mixed with Si NP and binder and deposited onto the copper collector via air-controlled electrospray, which was used as the anode. Based on the TGA results, the silicon content for all the Si/rGO anodes with six different rGO particles was almost the same, ~60wt% (see Figure S2). CrGO_7, due to the presence of some functional groups, starts to combust earliest, whereas PrGO_25 and PrGO_80 have the least functional groups combusts at the last. Fig. 6 shows the top-view SEM images of the Si/rGO electrode obtained via air-controlled electrospraying. It was observed that rGO with a small lateral dimension (CrGO_7 (Fig. 6a), TrGO_5 (Fig. 6b), and PrGO_7 (Fig. 6d)) resulted in the formation of Si clusters on the surface of the rGO sheets, exposing the Si particles. Interestingly, rGO with a large lateral dimension (PrGO_80 in Fig. 6f) also exhibits significant aggregation of Si particles on the surface of the rGO sheets. This is possibly due to the difficulty involved in dispersing and spraying large graphene sheets and the size imbalance between the Si nanoparticles and rGO. On the other hand, Si/rGO anodes with intermediate lateral dimensions (TrGO_20 Fig. 6c and PrGO_25 Fig. 6e) show that the Si particles are evenly distributed on the surface of rGO. Hence, it can be surmised that regardless of the reduction method, the size of the rGO particles plays a pivotal role in controlling the assembly of Si particles and rGO in the Si/rGO anode.

The internal morphology of the Si/rGO anodes with various rGO particles was also investigated. As demonstrated in Figure S4, all of the Si/rGO anodes exhibited sandwich structures where Si particles were placed between the rGO sheets. Fig. 7 shows the corresponding high-magnification cross-sectional SEM images. It is observed that the anode with PrGO_25 in Fig. 7e) shows Si particles nicely layered between the graphene sheets, showing the advantage of having a layered appearance due to plasma reduction, while an-

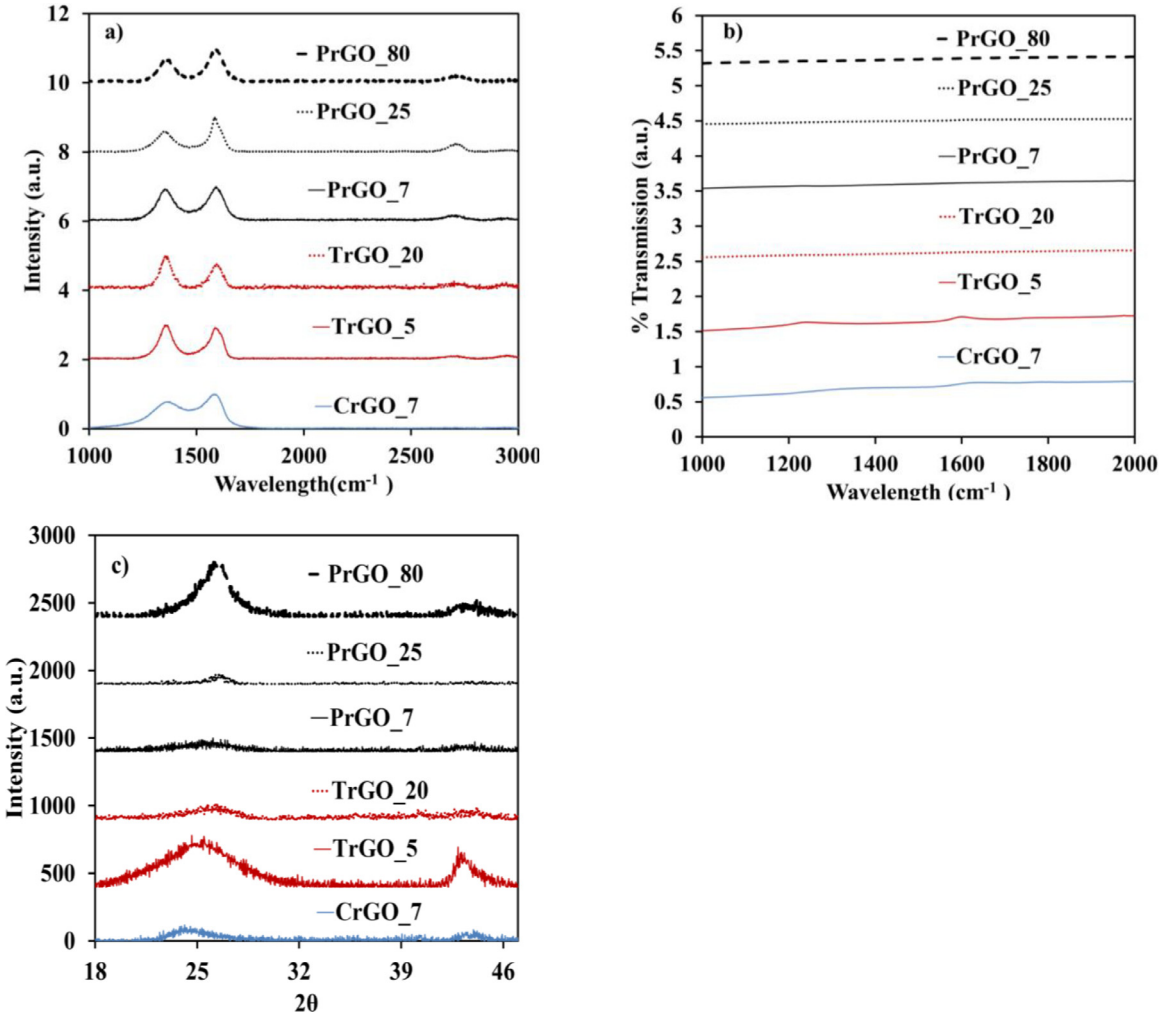

Fig. 4. a) Raman spectra, b) FTIR spectra, and c) XRD pattern of all the rGO particles used in this study.

odes with CrGO or TrGO particles and/or rGOs with small lateral dimensions (Figs. 7a) – e) exhibit less prominent sandwich structures. The anode with PrGO_80 in Fig. 7(f) shows a morphology similar to that of PrGO_25, although it does not provide precise layering because of the very large size of the PrGO_80 graphene sheets.

To test the effect of the different rGO particles on the electrochemical performance of the Si/rGO hybrid anode, we first carried out the cyclic voltammetry at the scan rate of 1 mV/s from 0.01 V to 1.5 V versus Li/Li$^+$. Fig. 8(a) shows the CV results of the six Si/rGO anodes for the 1st cycle. There is a small peak at 1.1 V, on the cathodic side, which is associated with the reduction of the electrolyte and irreversible formation of the SEI layer [56]. For CrGO_7 shown in blue, we observe a prominent peak at 0.4 V, which is not present in other rGO systems, which could be due to the irreversible reaction on the carbon surface induced by the oxygen functional groups present in CrGO_7 because carbonaceous impurities play an important role in the electrochemical activity of rGO [57,58]. An intense peak at 0.01 V is observed for all the Si/rGO anodes, which is associated with the formation of Li-Si alloys. On the anodic side we observe 2 characteristic peaks at 0.3 V and 0.52 V which are associated with the de-lithiation of the Li-Si alloys. Interestingly, PrGO_80 and PrGO_25 (black lines) show a much sharper peak at ~ 0.3 V which is not as sharp as that of the other rGO systems used in this study. This could promote faster kinetics for Li-ion de-insertion. The difference in the CV curves for CrGO_7 and PrGO_80 highlight the influence of using a particular rGO [59,60]. In the next cycle, the SEI peak disappears, as shown in Fig. 8(b), and the current intensity increases owing to the previously unreacted silicon that takes part in the reactions. This corresponds well with existing literature [61,62]. Fig. 8(c) shows a comparison of the 1st cycle capacity-voltage profiles of all the Si/rGO anodes. It displays a flat plateau, typical for Si/rGO anodes, around 0.25 V for the de-lithiation curve which corresponds to the formation of amorphous phase of Li_xSi from crystalline Si representing the alloying process [63]. Fig. 8(d) illustrates a comparison of the initial reversible capacity and initial Coulombic efficiency (ICE) for all six Si/rGO anodes. Anodes with TrGO_5 and PrGO_7 show the highest capacity, based on the entire weight of the electrode including the binder and rGO, of 1599.5 mAh/g and 1581.82 mAh/g respectively, possibly because of their smaller size that helps in better activation of Si, whereas TrGO_20 shows the least capacity of 1483.09 mAh/g, probably due to its structural defects leading to inactivated silicon, as can be observed in Fig. 7c). PrGO_80 shows the highest ICE of 84%, which is much higher than the previously reported ICE for Si/rGO system [64–67], because it has fewer defects and fewer oxygen functional groups, as well as larger lateral dimensions reducing the side reactions, whereas CrGO_7 shows the least ICE because of the presence of oxygen functional groups, as seen in Fig. 4b). This aligns well with the CV results shown in Fig. 8(a). After one cycle at 0.1C, 0.2C and 0.3C each, we carried out galvanostatic charging/discharging for 150 cycles at 0.3C,

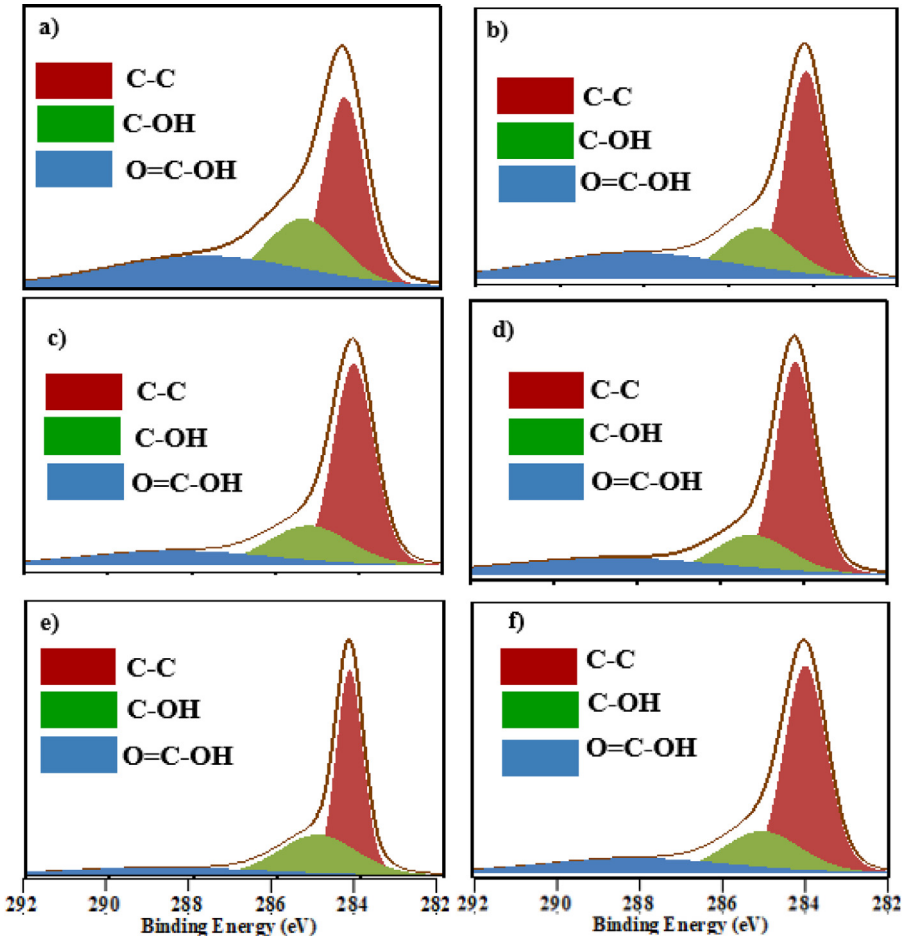

Fig. 5. High Resolution XPS spectra C1s a) CrGO_7, b) TrGO_5, c) TrGO_20, d) PrGO_7, e) PrGO_25, and f) PrGO_80.

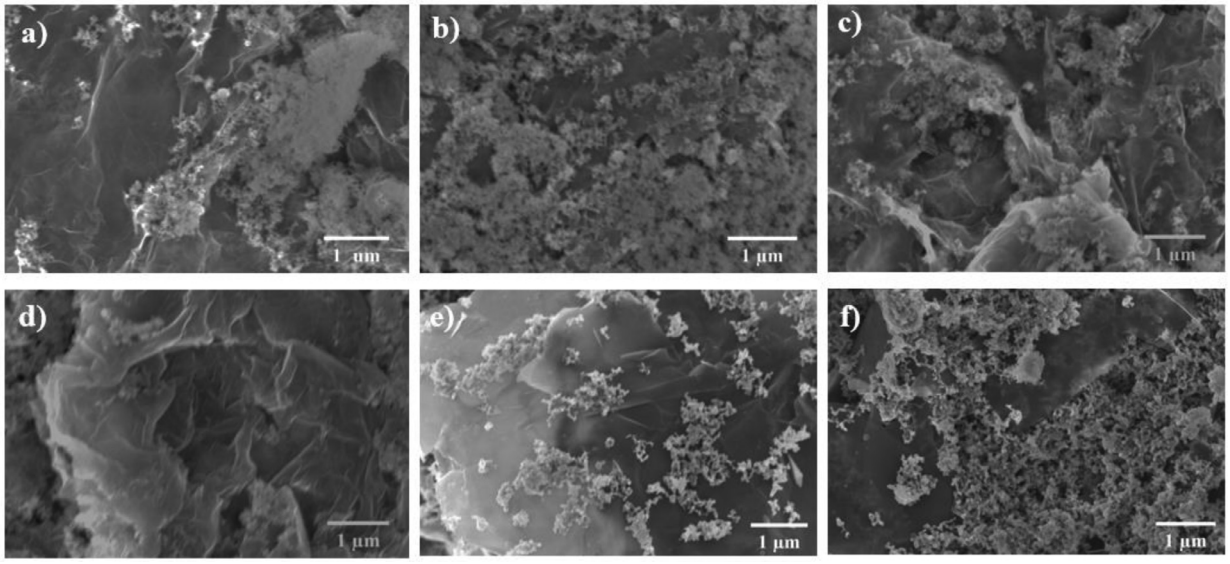

Fig. 6. Top view SEM images of Si/rGO electrode for a) CrGO_7, b) TrGO_5, c) TRGO_20, d) PrGO_7, e) PrGO_25, and f) PrGO_80.

and the results are plotted in Fig. 8e). Even though all Si/rGO anodes initially showed stable cycling behavior, CrGO_7 and PrGO_7 started to decline sharply after 50 to 70 cycles, whereas PrGO_25, PrGO_80, and TrGO_5 showed a great retention of 69% even after 150 cycles. This could be attributed to the high sphericity of these rGO particles, which helps mitigate the pulverization of the electrode structure due to its uniform coverage of the silicon nanoparticles and efficient packing, as shown in Fig. 1, whereas CrGO_7 and PrGO_7 have an irregular rGO shape and thus low sphericity and high aspect ratio. Postmortem SEM analysis was carried out after electrochemical cycling at 0.3C in Figure S6. We can see that the morphology of TrGO_5, PrGO_25 and PrGO_80 is largely pre-

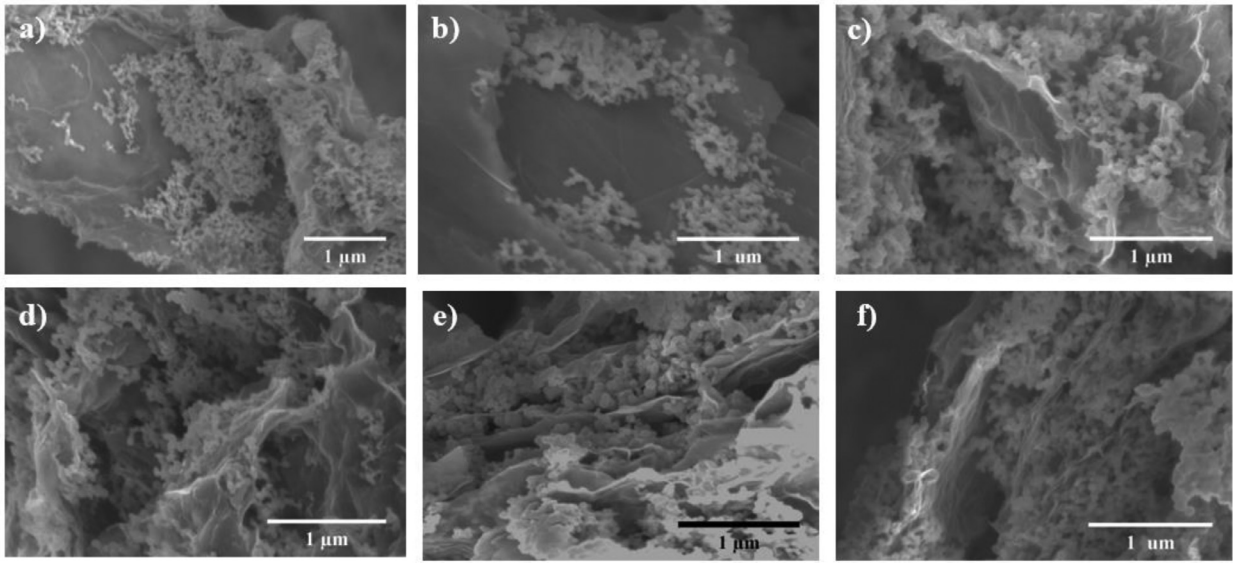

Fig. 7. High Magnification Cross-section SEM images of Si/rGO electrode for a) CrGO_7, b) TRGO_5, c) TRGO_20, d) PRGO_7, e) PrGO_25, and f) PrGO_80.

served after 150 cycles at 0.3C charge/discharge whereas CrGO_7 and PrGO_7 displayed prominent cracking.

In all figures, blue, red, and black lines were used for CrGO, TrGO, and PrGO, respectively, and thicker red and black lines were used for TrGO and PrGO with larger particle sizes.

Because in this work, we are not using any conductive additives, it is extremely important for the rGO to be conductive. The bulk resistivity was measured via simple four-point probe tests, which were carried out by electrospraying all six rGO solutions in water, along with the dispersant, onto silicon wafers. Table 1 lists the values of the bulk resistivities of the six rGO sheets, which is the average of the values taken at five different points on the Si wafer. Impressively, both PrGO_25 and PrGO_80 rGO exhibited one order of magnitude lower resistivity than any other rGO system, further validating our Raman and XPS findings, whereas TrGO_5 showed the highest resistivity, possibly due to a combination of functional groups and graphitic defects. Fig. 9(a) shows the electrochemical impedance spectroscopy (EIS) for all six Si/rGO anodes before cycling. All the Si/rGO electrodes show a semicircle corresponding to the charge transfer resistance at the electrode-electrolyte interface and a sloping line representing Warburg diffusion [67–69]. We note that PrGO_25 showed the lowest overall charge transfer resistance, whereas TrGO_5 showed the highest charge transfer resistance, almost twice as much as PrGO_25, showing that the higher electrical resistance of rGO translates to a higher charge transfer resistance. It is worth mentioning that PrGO_80 also showed a relatively low resistance. Fig. 9b) shows the rate capability performance of all six Si/rGO anodes. At milder currents, such as 0.1C, we see similar performance as seen in Fig. 8e), but at higher currents, especially at 2C, we can see that PrGO_25 and PrGO_80 comfortably outperform the rest of the rGO system delivering ~ 1000 mAh/g and 850, respectively, at 2C/2C rates. TrGO_5 showed the worst performance at 2C/2C, which can be seen as a combination of the large charge transfer resistance of TrGO_5 and the reduction of the ionic mobility of the Li ions at faster rates in a highly compressed, wrinkled, graphenic structure of TrGO_5, as shown in Fig. 2b). This exemplifies the importance of having highly conductive rGO sheets for Si anodes for fast-charging electrodes. We also note that all Si/rGO electrodes can recover their original capacity at 0.1 C, further highlighting the effectiveness of the conductive rGO. Thus far, it is evident that plasma-reduced graphene oxide shows a much better rate capability compared to other rGO systems. To elucidate the effect of the size of the lateral dimension of the graphene sheet on lithium-ion diffusion and the eventual rate capability, the rate capabilities of all three plasma rGO particles were compared (Fig. 9c). We observe that there seems to be an optimum size of the rGO flake for enhanced rate capability. PrGO_25 gave the best performance, whereas PrGO_7 was the worst of the three. In order to understand the difference in rate capability between PrGO_25 and PrGO_80, SEM and EDX of the electrode structure were carried out as shown in Figure S5. Figure S3 (a) and (b) show the top view and magnified image of the electrode structure of Si/PrGO_25. We can see that there is uniform coverage of Si, whereas in the corresponding images for Si/PrGO_80 shown in Figure S3 c) and d) there are many exposed Si clusters on the graphene sheet. This could be due to the very large lateral dimensions of PrGO_80, which makes it difficult to disperse and form layered structures. The Si coverage was further quantified by EDX, as shown in Figure S5. S5 a) and b) show the EDX layered mapping of Si/PrGO_25 and the corresponding map sum spectra images. This shows uniform carbon coverage. However, the corresponding EDX layered mapping and map sum spectra for the Si/PrGO_80 electrode shown in Figure S5 c) and d) clearly show a large amount of Si exposure, especially compared to Si/PrGO_25. This lack of uniform coverage of Si in the case of Si/PrGO_80 results in a lower rate capability compared to Si/PrGO_25. Finally, Fig. 9(d) shows the cycling of Si/rGO at 1C/1C rates. The testing conditions were kept the same, that is, 1st cycle at 0.1C, 2nd at 0.2C, 3ed at 0.3C, and then 100 cycles at 1C/1C rates. We observed peculiar behavior with PrGO_25. Initially, PrGO_25 starts off at a much higher capacity at 1C currents but over cycles, it suffers a drop in its capacity, whereas the anodes with all the other rGO systems are stable. This could probably be due to the higher conductivity and superior Li-ion transport of PrGO_25, which results in a higher capacity even at 1C, yielding over 1000 mAh/g capacity after 100 cycles. Although its initial capacity is lower than that of the anode with PrGO_25, the anode with PrGO_80 retained its superior performance, delivering a capacity of 865 mAh/g after 100 cycles, resulting in an excellent retention of 93%. The rGO particles used in this study showed much lower capacities than those of PrGO_25 and PrGO_80 at 1C.

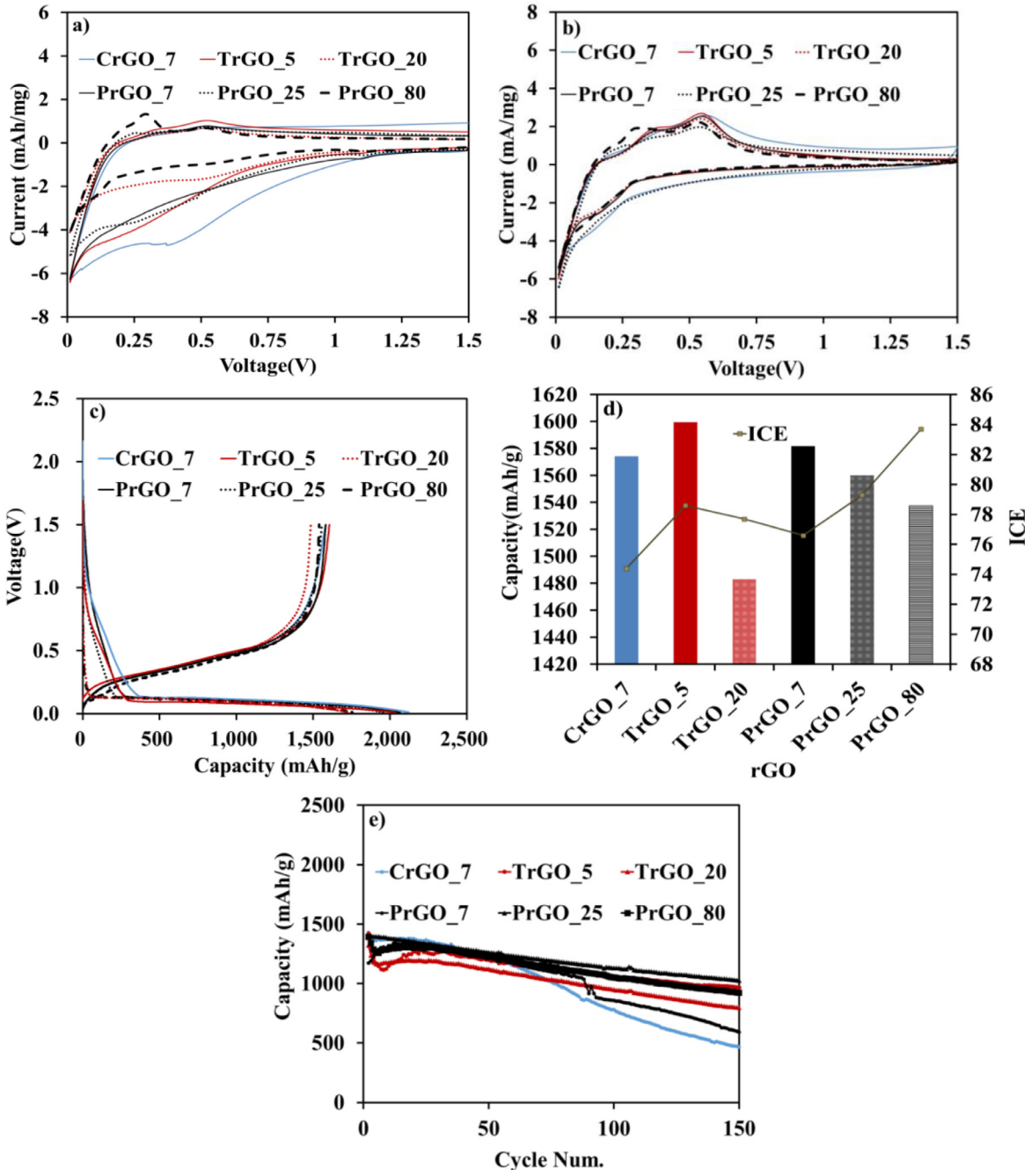

Fig. 8. a) CV curves for 1st cycle b) CV curves for 2nd cycle c) Initial capacity-voltage curve d) Combined plot of ICE, discharge Capacity e) cycle performance tested at 0.3C for Si/rGO (CrGO_7, TrGO_5, TrGO_20, PrGO_7, PrGO_25, and PRGO_80) electrodes.

4. Conclusion

In summary, we have carried out a comprehensive study to identify the contributions of rGO microsheets to the performance of Si/rGO anodes by comparing the properties of six different rGO particles and their hybrid anodes with Si particles. The quality of a particular rGO is very much dependent on its reduction, and this quality of rGO is further linked to the electrochemical behavior of the widely used Si/rGO electrodes for Li-ion batteries. We found that not only the quality but also the size and sphericity of the rGO particles are important factors. Our results revealed that a smaller size of rGO gave higher initial capacities; for example, TrGO_5 exhibited a reversible capacity of 1600 mAh/g due to better activation of Si. We demonstrated that a higher ICE (84% for PrGO_80) can be obtained by reducing the defects of rGO and removing the oxygen functional groups. TrGO_5, PrGO_25, and PrGO_80 showed excellent retention at 0.3C suggesting that a higher degree of sphericity offers a more uniform control over Si volume expansion, and thus prevents pulverization of the electrode structure. Furthermore, the importance of the electrical conductivity of rGO is highlighted by the excellent performance of PrGO_25 and PrGO_80 at 1C, giving a reversible capacity of ~ 1000 mAh/g and 865 mAh/g after 100 cycles, respectively. Overall, plasma reduced graphene oxide systems were found to give the best performance, and thus the effect of the lateral dimension of the plasma-reduced graphene oxide on the rate capability was studied. PrGO_25 was found to be the optimum rGO in our study to satisfy all the requirements expected for a Si/rGO electrode efficiently. The current study can

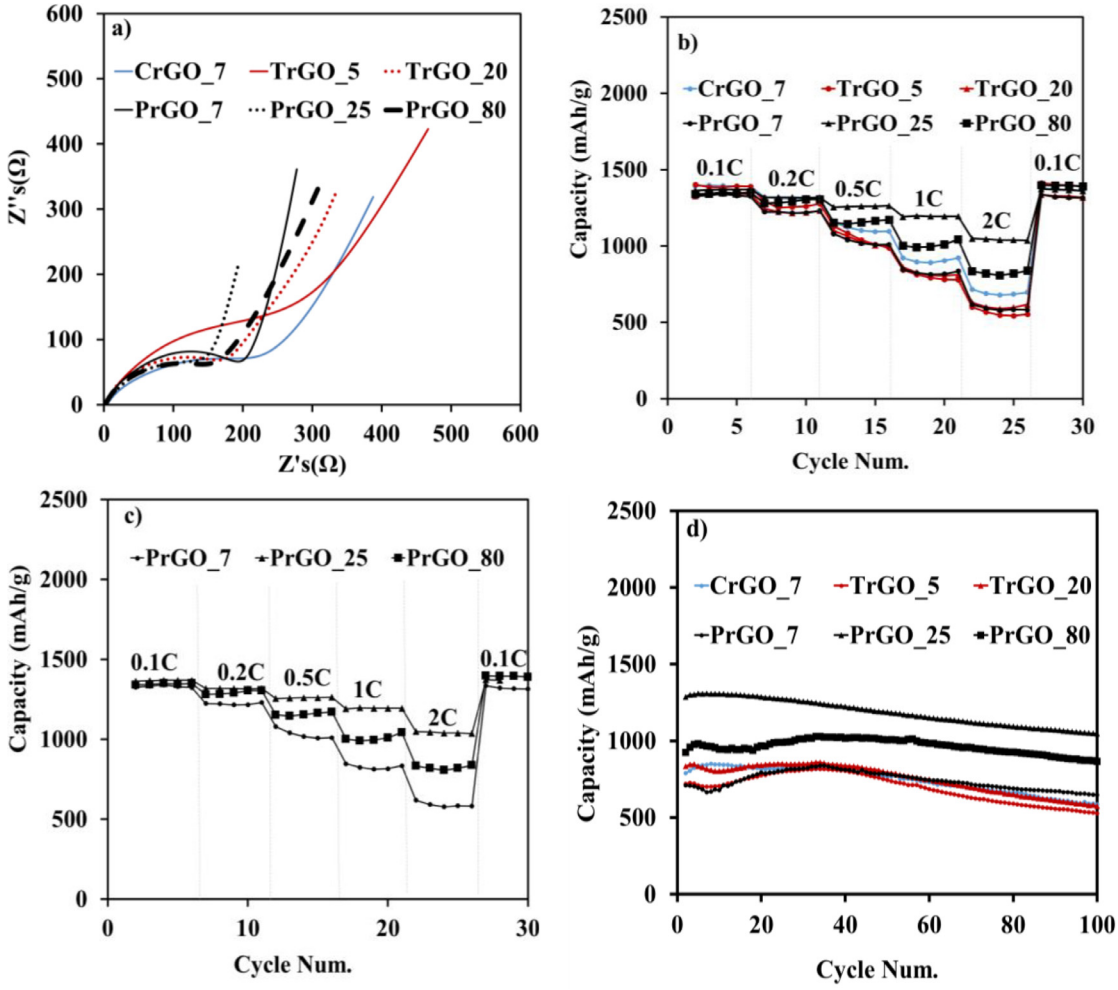

Fig. 9. a) Nyquist Plots b) Rate capability (CrGO_7, TrGO_5, TrGO_20, PrGO_7, PrGO_25, PrGO_80) c) Rate Capability (PrGO_7, PrGO_25, PrGO_80) d) cycle performance tested at 1C for Si/rGO electrodes.

open the door for tailored manufacturing rGO particles towards specific applications and provide a guiding light towards selecting the right kind of rGO for different assemblies of Si/rGO electrode systems.

Credit author statement

Yash Joshi worked on methodology and characterization, cell tests, data analysis as well as writing the original draft, reviewing and editing. **Avinash Umasankaran** focused on spray experiments and anode preparations, while **Christopher Klaassen** contributed to characterization (TEM and posimetry), and battery testing, as well as reviewing and editing the manuscript. **Mohammed AlAmer** prepared and characterized (electrical conductivity) of rGO samples, as well as reviewing and editing the manuscript, and finally, **Yong Lak Joo**, corresponding author, conceptualized and supervised the current work as well as reviewing and revising the manuscript.

Declaration of Competing Interest

The authors declare no competing financial interest.

Acknowledgment

This work used the Cornell Center of Materials Research (CCMR) Shared Facilities, which are supported by the NSF MRSEC program (DMR-1719875). This work was also partially supported by Dongjin Semichem, LTD., and JMC Corp. via the CCMR INVEST Program.

Supplementary materials

Supplementary material associated with this article can be found, in the online version, at doi:10.1016/j.electacta.2021.139753.

References

[1] M. Armand, J.M. Tarascon, Building better batteries, Nature 451 (2008) 652–657.
[2] B. Dunn, H. Kamath, J. Tarascon, Electrical Energy Storage for the Grid : a Battery of Choices, Science 334 (2011) 928–936.
[3] P. Bruce, G. Scrosati, J. Tarascon, Lithium Batteries Nanomaterials for Rechargeable Lithium Batteries, Angewandte 47 (2008) 2930–2946.
[4] M. Li, J. Lu, Z.Chen, K. Amine, 30 Years of lithium-ion batteries. 1800561 (2018) 1–24.
[5] X. Zuo, J. Zhu, P. Müller-buschbaum, Y. Cheng, Nano Energy Silicon based lithium-ion battery anodes : a chronicle perspective review, Nano Energy 31 (2017) 113–143.
[6] M. Ashuri, Q. He, L.L. Shaw, Silicon as a potential anode material for Li-ion batteries: where size, geometry and structure matter, Nanoscale 8 (2016) 74–103.
[7] J.Y. Li, Q. Xu, G. Li, Y.X. Yin, L.J. Wan, Y.G. Guo, Research progress regarding Si-based anode materials towards practical application in high energy density Li-ion batteries, Mater. Chem. Front. 1 (2017) 1691–1708.
[8] K. Feng, M. Li, W. Liu, A.G. Kashkooli, X. Xiao, M. Cai, Z. Chen, Silicon-Based Anodes for Lithium-Ion Batteries: from Fundamentals to Practical Applications, Small 14 (2018) 170237.
[9] D. Ma, Z. Cao, A. Hu, Si-based anode materials for li-ion batteries: a mini review, Nano-Micro Lett 6 (2014) 347–358.

[10] W.J. Zhang, A review of the electrochemical performance of alloy anodes for lithium-ion batteries, J. Power Sources 196 (2011) 13–24.
[11] K.M. Abraham, Prospects and limits of energy storage in batteries, J. Phys. Chem. Lett. 6 (2015) 830–844.
[12] E. Environ, J. Szczech, S. Jin, Nanostructured silicon for high capacity lithium battery anodes, Energy Environ. Sci. 1 (2011) 56–72.
[13] N.S. Hochgatterer, M.R. Schweiger, S. Koller, P.R. Raimann, T. Wöhrle, C. Wurm, M. Winter, Silicon /graphite composite electrodes for high-capacity anodes : influence of binder chemistry on cycling stability, Electrochem. Solid-State Lett. 11 (2008) 76–80.
[14] J.P. Maranchi, A.F. Hepp, P.N. Kumta, High Capacity, Reversible Silicon Thin–Film Anodes for Lithium-Ion Batteries, Electrochem. Solid-State Lett. 6 (2003) 198–201.
[15] H. Wu, Y. Cui, Designing nanostructured Si anodes for high energy, Nano Today 7 (2012) 414–429.
[16] L.Y. Beaulieu, K.W. Eberman, R.L. Turner, L.J. Krause, Colossal reversible volume changes in lithium alloys, Electrochem. Solid-State Lett. 4 (2001) 7–10.
[17] J.H. Ryu, J.W. Kim, Y. Sung, S.M. Oh, Failure modes of silicon powder negative electrode in lithium secondary batteries, Electrochem. Solid-State Lett. 7 (2004) 306–309.
[18] Y. Oumellal, N. Delpuech, D. Mazouzi, N. Dupré, P. Soudan, B. Lestriez, D. Guyomard, The failure mechanism of nano-sized Si-based negative electrodes for lithium ion batteries, J. Matter. Chem. 21 (2011) 6201–6208.
[19] C.K. Chan, H. Peng, G. Liu, K. Mcllwrath, X.F. Zhang, R.A. Huggins, Y. Cui, High-performance lithium battery anodes using silicon nanowires, Nat. Nanotech 3 (2007) 31–35.
[20] H. Kim, M. Seo, M.H. Park, J. Cho, A critical size of silicon nano-anodes for lithium rechargeable batteries, Angew. Chemie - Int. Ed. 49 (2010) 2146–2149.
[21] X.H. Liu, L. Zhong, S. Huang, S.X. Mao, T. Zhu, J.Y. Huang, Size-dependent fracture of silicon nanoparticles during lithiation, ACS Nano 6 (2012) 1522–1531.
[22] H. Tian, F. Xin, X. Wang, W. He, W. Han, High capacity group-IV elements (Si, Ge, Sn) based anodes for lithium-ion batteries, J. Mater. 1 (2015) 153–169.
[23] Y. Hwa, W.S. Kim, S.H. Hong, H.J. Sohn, High capacity and rate capability of core-shell structured nano-Si/C anode for Li-ion batteries, Electrochim. Acta 71 (2012) 201–205.
[24] T.H. Hwang, Y.M. Lee, B.S. Kong, J.S. Seo, J.W. Choi, Electrospun core-shell fibers for robust silicon nanoparticle-based lithium ion battery anodes, Nano Lett. 12 (2012) 802–807.
[25] Y. Zhou, H. Guo, Y. Yong, Z. Wang, X. Li, R. Zhou, Introducing reduced graphene oxide to improve the electrochemical performance of silicon-based materials encapsulated by carbonized polydopamine layer for lithium ion batteries, Mater. Lett. 195 (2017) 164–167.
[26] Z. Liu, P. Guo, B. Liu, W. Xie, D. Liu, D. He, Carbon-coated Si nanoparticles/reduced graphene oxide multilayer anchored to nanostructured current collector as lithium-ion battery anode, Appl. Surf. Sci. 396 (2017) 41–47.
[27] F. Maroni, R. Raccichini, A. Birrozzi, G. Carbonari, R. Tossici, F. Croce, R. Marassi, F. Nobili, Graphene/silicon nanocomposite anode with enhanced electrochemical stability for lithium-ion battery applications, J. Power Sources 269 (2014) 873–882.
[28] L. Fei, B.P. Williams, S.H. Yoo, J. Kim, G. Shoorideh, Y.L. Joo, Graphene folding in Si rich Carbon Nanofibers for Highly Stable, High Capacity, Li-ion battery anodes, ACS Appl. Mater. Interfaces 8 (2016) 5243–5250.
[29] L. Fei, S.H. Yoo, R.A. Villamayor, B.P. Williams, S.Y. Gong, S. Park, K. Shin, Y.L. Joo, Graphene Oxide Involved Air-Controlled Electrospray for Uniform, Fast, Instantly Dry, and Binder-Free Electrode Fabrication, ACS Appl. Mater. Interfaces 9 (2017) 9738–9746.
[30] Y. Joshi, S. Zamani, C. Klaassen, Y.L. Joo, Mitigation and in-situ probing of volume expansion in silicon/graphene hybrid anodes for high capacity, high rate capable lithium-ion batteries, Adv. Energy Sustain. Res. 2100 (2021) 202100125.
[31] A.P. Kauling, A.T. Seefeldt, D.P. Pisoni, R.C. Pradeep, R. Bentini, R.V. O.liviera, K.S. Novoselov, A.H. Castro Neto, The worldwide graphene flake production, Adv. Mater. 30 (2018) 1803784.
[32] M. Tokur, M.Y. Jin, B.W. Sheldon, H. Akbulut, Stress bearing mehcanism of reduced graphene oxide in silicon-based anodes for lithium ion batteries, ACS Appl. Mater. Interfaces 12 (2020) 33855–33869.
[33] Z. Benzait, N. Yuca, Synergistic effect of carbon nanomaterials on a cost-effective coral-like Si/rGO composite for lithium ion battery application, Electrochemica Acta 339 (2020) 135917.
[34] X. Zhou, Y.X. Yin, L.J. Wan, Y.G. Guo, Facile synthesis of silicon nanoparticles inserted into graphene sheets as improved anode materials for lithium-ion batteries, Chem. Commun. 48 (2012) 2198–2200.
[35] H. Tang, J.P. Tu, X.Y. Liu, Y.J. Zhang, S. Huang, W.Z. Li, X.L. Wang, C.D. Gu, Self-assembly of Si/honeycomb reduced graphene oxide composite film as a binder-free and flexible anode for Li-ion batteries, J. Matter. Chem. A. 2 (2014) 5834–5840.
[36] N. Lin, J. Zhou, L. Wang, Y. Zhu, Y. Qian, Polyaniline-assisted synthesis of Si@C/RGO as anode material for rechargeable lithium-ion batteries, ACS Appl. Mater. Interfaces 7 (2015) 409–414.
[37] F. Sun, K. Huang, X. Qi, T. Gao, Y. Liu, X. Zou, X. Wei, J. Zhong, A rationally designed composite of alternating strata of Si nanoparticles and graphene: a high-performance lithium-ion battery anode, Nanoscale 5 (2013) 8586–8592.
[38] W.J. Meng, X.Y. Han, Y. Hou, Y. Xie, J. Zhang, C.J. He, D.L. Zhao, Defect-Repaired reduced graphene oxide caging silicon nanoparticles for lithium-ion anodes with enhanced reversible capacity and cyclic performance, Electrochemica Acta 382 (2021) 138271.
[39] Y. Cen, R. Sisson, Q. Qin, J. Liang, Current Progress of Si/Graphene Nanocomposites for Lithium-Ion Batteries, C 4 (2018) 18.
[40] M.J. Divvela, R. Zhang, Y. Zhmayev, S. Pinge, J.H. Lee, S.W. Kim, Y.L. Joo, Control of formation of viscoelastic droplets and distribution of nano-inclusions in functional deposition for lithium sulfur batteries, Soft Matter 15 (2019) 6485–6494.
[41] A.C. Ferrari, Ramspectroscopy of graphene and graphite: disorder, electron-phonon coupling, doping and nonadiabatic effects, Solid State Commun. 143 (2007) 47–57.
[42] L.G. Cançado, A. Jorio, E.H. Ferreira, F. Stavale, C.A. Achete, R.B. Capaz, M.V.O. Moutinho, A. Lombardo, T.S. Kulmala, A.C. Ferrari, Quantifying defects in graphene via Raman spectroscopy at different excitation energies, Nano Lett. 11 (2011) 3190–3196.
[43] A. Eckmann, A. Felten, A. Mishchenko, L. Britnell, R. Krupke, K.S. Novoselov, C. Casiraghi, Probing the nature of defects in graphene by Raman spectroscopy, Nano Lett. 12 (2012) 3925–3930.
[44] R. Saito, in: Raman Spectroscopy of Graphene Edges, World Scientific Publishing Co, 2011, pp. 91–103.
[45] R. Beams, L. Gustavo Cançado, L. Novotny, Raman characterization of defects and dopants in graphene, J. Phys. Condens. Matter 27 (2015) 25634863.
[46] V.T. Nguyen, H.D. Le, V.C. Nguyen, T.T. Ngo, D.Q. Le, X.N. Nguyen, N.M. Phan, Synthesis of multi-layer graphene films on copper tape by atmospheric pressure chemical vapor deposition method, Adv. Nat. Sci. Nanosci. Nanotechnol. 4 (2013) 035012.
[47] K. Satheesh, R. Jayavel, Synthesis and electrochemical properties of reduced graphene oxide via chemical reduction using thiourea as a reducing agent, Mater. Lett. 113 (2013) 5–8.
[48] M. Strankowski, D. Włodarczyk, L. Piszczyk, J. Strankowska, Polyurethane Nanocomposites Containing Reduced Graphene Oxide, FTIR, Raman, and XRD Studies, J. Spectrosc. 2016 (2016) 7520741.
[49] H.J. Lee, J.S. Kim, K.Y. Lee, K.H. Park, J.S. Bae, M. Mubarak, H. Lee, Elucidation of an intrinsic parameter for evaluating the electrical quality of graphene flakes, Sci. Rep. 9 (2019) 1–8.
[50] N. Morimoto, T. Kubo, Y. Nishina, Tailoring the oxygen content of graphite and reduced graphene oxide for specific applications, Sci. Rep. 6 (2016) 4–11.
[51] S.M. Tan, A. Ambrosi, C.K. Chua, M. Pumera, Electron transfer properties of chemically reduced graphene materials with different oxygen contents, J. Mater. Chem. A 2 (2014) 10668–10675.
[52] B. Gupta, N. Kumar, K. Panda, V. Kanan, S. Joshi, I.V. Fisher, Role of oxygen functional groups in reduced graphene oxide for lubrication, Sci. Rep. 7 (2017) 1–14.
[53] R. Muzyka, S. Drewniak, T. Puselny, M. Chrubasik, G. Gryglewicz, Characterization of graphite oxide and reduced graphene oxide obtained from different graphite precursors and oxidized by different methods using Raman spectroscopy, Materials (Basel) 11 (2018) 15–17.
[54] S. Some, Y. Kim, Y. Yoon, H. Yoo, S. Lee, Y. Park, H. Lee, High-quality reduced graphene oxide by a dual-function chemical reduction and healing process, Sci. Rep. 3 (2013) 1–5.
[55] M. Choi, J.C. Kim, D.W. Kim, Waste Windshield-Derived Silicon/Carbon Nanocomposites as High-Performance Lithium-Ion Battery Anodes, Sci. Rep. 8 (2018) 1–12.
[56] T. Ikonen, T. Nissinen, E. Pohjalainen, O. Sorsa, T. Kallio, V.P. Lehto, Electrochemically anodized porous silicon: towards simple and affordable anode material for Li-ion batteries, Sci. Rep. 7 (2017) 1–8.
[57] M. Pumera, Electrochemistry of graphene, graphene oxide and other graphenoids: review, Electrochem. Commun. 36 (2013) 14–18.
[58] L. Tang, Y. Wang, Y. Li, H. Feng, J. Lu, J. Li, Preparation, structure, and electrochemical properties of reduced graphene sheet films, Adv. Funct. Mater. 19 (2009) 2782–2789.
[59] Q. Pan, P. Zuo, S. Lou, T. Mu, C. Du, X. Cheng, Y. Ma, Y. Gao, G. Yin, Micro-sized spherical silicon@carbon@graphene prepared by spray drying as anode material for lithium-ion batteries, J. Alloys Compd. 723 (2017) 434–440.
[60] R. Hu, W. Sun, Y. Chen, M. Zeng, M. Zhu, Silicon/graphene based nanocomposite anode: large-scale production and stable high capacity for lithium ion batteries, J. Mater. Chem. A 2 (2014) 9118–9125.
[61] W. Sun, R. Hu, H. Zhang, Y. Wang, L. Yang, J. Liu, M. Zhu, A long-life nano-silicon anode for lithium ion batteries: supporting of graphene nanosheets exfoliated from expanded graphite by plasma-assisted milling, Electrochim. Acta 187 (2016) 1–10.
[62] G. Wang, X. Shen, J. Yao, J. Park, Graphene nanosheets for enhanced lithium storage in lithium ion batteries, Carbon N. Y. 47 (2009) 2049–2053.
[63] M. Liang, L. Zhi, Graphene-based electrode materials for rechargeable lithium batteries, J. Mater. Chem. 19 (2009) 5871–5878.
[64] Y.C. Zhang, Y. You, S. Xin, Y.X. Yin, J. Zhang, P. Wang, X.S. Zheng, F.F. Cao, Y.G. Guo, Rice husk-derived hierarchical silicon/nitrogen-doped carbon/carbon nanotube spheres as low-cost and high-capacity anodes for lithium-ion batteries, Nano Energy 25 (2016) 120–127.
[65] K. Zhang, Y. Xia, Z. Yang, R. Fu, C. Shen, Z. Liu, Structure-preserved 3D porous silicon/reduced graphene oxide materials as anodes for Li-ion batteries, RSC Adv. 7 (2017) 24305–24311.
[66] B.L. He, B. Dong, H.L. Li, Preparation and electrochemical properties of Ag-mod-

ified TiO2 nanotube anode material for lithium-ion battery, Electrochem. Commun. 9 (2007) 425–430.
[67] S.S. Zhang, K. Xu, T.R. Jow, Electrochemical impedance study on the low temperature of Li-ion batteries, Electrochim. Acta 49 (2004) 1057–1061.
[68] M. Zhang, Y. Li, E. Uchaker, S. Candelaria, L. Shen, T. Wang, G. Cao, Homogenous incorporation of SnO2 nanoparticles in carbon cryogels via the thermal decomposition of stannous sulfate and their enhanced lithium-ion intercalation properties, Nano Energy 2 (2013) 769–778.
[69] X. Pu, M. Liu, L. Li, C. Zhang, Y. Pang, C. Jiang, L. Shao, W. Hu, Z.L. Wang, Efficient charging of Li-ion batteries with pulsed output current of triboelectric nanogenerators, Adv. Sci. 3 (2015) 1–7.